Materials and Design 144 (2018) 192–208

Contents lists available at ScienceDirect

Materials and Design

journal homepage: www.elsevier.com/locate/matdes

Tailoring columnar microstructure of axial suspension plasma sprayed TBCs for superior thermal shock performance

Ashish Ganvir [a,*], Shrikant Joshi [a], Nicolaie Markocsan [a], Robert Vassen [b]

[a] University West, 46186 Trollhättan, Sweden
[b] Forschungszentrum Jülich GmbH, IEK-1, 52425 Jülich, Germany

HIGHLIGHTS

- A novel design strategy for tailoring ASPS columnar microstructure is proposed.
- Porosity is classified in 4 classes: (>10 μm), (10 μm–1 μm), (1 μm–100 nm) & (<100 nm).
- About 40%(1 μm–100 nm), 34%(10 μm–1 μm), 20%(>10 μm) & 7%(<100 nm) pores were present.
- Fracture toughness was found to be the most prominent life-determining factor.
- Pores (>10 μm) had the most severe effect on lifetime than other porosity classes.

GRAPHICAL ABSTRACT

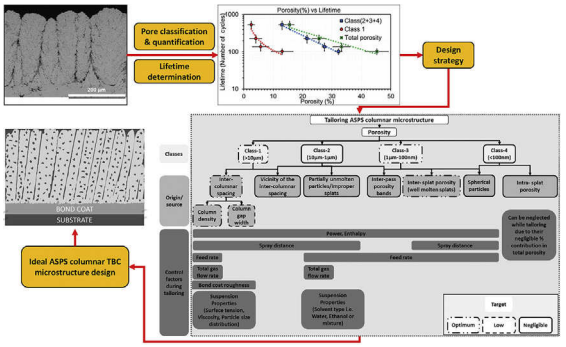

ARTICLE INFO

Article history:
Received 1 December 2017
Received in revised form 1 February 2018
Accepted 3 February 2018
Available online 4 February 2018

Keywords:
Suspension plasma spraying
Thermal barrier coatings
Thermal shock lifetime
Superior performance
Pore size distribution
Fracture toughness

ABSTRACT

This paper investigates the thermal shock behavior of thermal barrier coatings (TBCs) produced by axial suspension plasma spraying (ASPS). TBCs with different columnar microstructures were subjected to cyclic thermal shock testing in a burner rig. Failure analysis of these TBCs revealed a clear relationship between lifetime and porosity. However, tailoring the microstructure of these TBCs for enhanced durability is challenging due to their inherently wide pore size distribution (ranging from few nanometers up to few tens of micrometers). This study reveals that pores with different length scales play varying roles in influencing TBC durability. Fracture toughness shows a strong correlation with the lifetime of various ASPS TBCs and is found to be the prominent life determining factor. Based on the results, an understanding-based design philosophy for tailoring of the columnar microstructure of ASPS TBCs for enhanced durability under cyclic thermal shock loading is proposed.

1. Introduction

Thermal barrier coatings (TBCs) are frequently used to provide thermal and oxidation protection to hot section components of gas turbine engines at high temperatures [1]. The performance of TBCs is measured by their ability to provide good thermal insulation and last long under harsh operating conditions [2,3]. The need to suppress degradation of TBCs due to various changes associated with sustained high temperature exposure, such as phase transformation, sintering, oxidation etc., has become more compelling as the operating temperature of gas turbines is being constantly increased to improve efficiency [4–6]. High temperature exposure under severe cyclic thermal shock conditions, as experienced during frequent take-off and landing of aero-engines,

* Corresponding author at: Department of Engineering Science, University West, Trollhättan 46186, Sweden.
E-mail addresses: ashish.ganvir@hv.se (A. Ganvir), shrikant.joshi@hv.se (S. Joshi), nicolaie.markocsan@hv.se (N. Markocsan), r.vassen@fz-juelich.de (R. Vassen).

https://doi.org/10.1016/j.matdes.2018.02.011

can accelerate premature failure of TBCs due to excessive thermal gradients and accompanying microstructural changes [7,8].

Microstructures of TBCs in actual use on hot-section components of aero turbine engines are of both lamellar [9] and columnar [10] type. The former is produced by atmospheric plasma spraying (APS) [9] and the latter by electron beam physical vapor deposition (EBPVD) [10]. APS sprayed lamellar TBCs are known to provide superior thermal insulation due to their inherent porous microstructure [11] whereas the EBPVD TBCs exhibit extended durability due to their strain tolerant columnar structure [3].

Suspension plasma spraying (SPS) is a relatively new technique which has been shown to produce a columnar microstructure as well as yield high porosity in the TBCs [12,13]. The suspension is typically comprised of fine particles (100 nm–5 μm) usually suspended in water or alcohol. Coatings built by the SPS process involve extremely fine droplets arising from fragmentation of a suspension stream resulting in small particles being exposed to the plasma plume in flight after solvent evaporation and depositing them on the bond coat asperities [13–15]. Column formation in SPS is reported to be related to the suspension droplet/particle's trajectory in flight and its momentum just prior to impact on the bond coat asperities, and the subsequent shadowing effect [14,15] due to the asperities of the bond coat. Hence, both the suspension properties (surface tension, viscosity, density etc.) as well as the plasma spray parameters (power, enthalpy, gas flow, spray distance etc.) have a crucial influence on the columnar microstructure, including the column density (number of columns per unit length) and overall porosity [13]. Under similar suspension conditions and plasma spray parameters, the column density has been found to be influenced by bond coat roughness, with smoother bond coats resulting in higher column density [16].

SPS sprayed TBCs with a porous columnar microstructure have been found promising for providing superior functional performance compared to conventional APS sprayed TBCs, yielding lower thermal conductivity [17], higher thermal cyclic fatigue (TCF) [12] and higher thermal shock lifetime [12]. High power axial suspension plasma spraying (ASPS) is a recent variant of the SPS technology which has been shown to enable a wide process window and is, thereby, capable of producing various types of columnar microstructures as well as porous, vertically cracked [18,19] and various function dependent coating architectures such as powder-suspension hybrid, composite and layered [20,21]. These microstructures produced by ASPS have not only resulted in a wide range of total porosity (from as low as 2–3% [20] to beyond 40% [18]) but also a wide pore size distribution, ranging from few nanometers to few tens of micrometers [18,19].

There is significant research interest in establishing a relationship between the microstructure and TCF as well as thermal shock lifetime in SPS/ASPS TBCs. Higher amount of porosity and presence of fine features (pores, grains etc.) in the microstructure have been reported to be mainly responsible for enhancing phonon scattering and, hence, reducing thermal conductivity [22]. However, it has also been suggested that these fine features may have a propensity to experience high temperature changes, such as sintering, hence making these microstructures unstable [17,23]. In addition, it has also been shown that high porosity, along with high column density, can improve TCF life due to enhanced strain tolerance [16]. Zhao et al. and Curry et al. have shown that such columnar microstructures can also provide higher thermal shock life [16,24]. Although, these columnar coatings have shown to provide high thermal shock lifetime [16,24], the reason why they do so has not been clearly stated. Moreover, optimization of the columnar microstructure for achieving the highest possible thermal shock life is difficult because the influence of overall porosity, pore size distribution, column density etc. on TBC durability is not yet very well understood. Prima facie, the inhomogeneous and wide pore size distribution in ASPS microstructures makes tailoring of microstructures appear particularly challenging. It is pertinent to point out that such understanding has already evolved in case of conventional APS TBCs where porosity and various microstructural features have been demonstrated to play a significant role on their thermal shock behavior. For example, high porosity and inhomogeneous distribution of pre-existing micro cracks and pores have been found to deteriorate thermal shock life whereas the presence of segmented vertical cracks and nanostructured features have been noted to enhance durability in similar conditions [25–27]. Tailoring APS microstructures by optimizing their porosity during processing has also been attempted, with process parameters such as input power, spray distance, powder feed rate etc. being found to be critical [28]. These studies have helped in developing reliable APS TBCs for high performance applications, motivating the need for a similar improved understanding of SPS TBCs to encourage their adoption by the industry.

The goal of this work was to study the influence of different ASPS TBCs with distinct columnar microstructures on their functional attributes as well as thermal shock life and, thereby, investigate the associated interdependencies. Four different TBCs with varying column density, porosity and pore-size distribution were produced and exposed to identical cyclic thermal shock loading conditions. Porosity was categorized in four different classes based on the pore size and the respective role of each on coating durability was assessed. Thermo-mechanical properties such as thermal conductivity, hardness, E-modulus, fracture toughness etc. were also experimentally measured for all coatings in order to comprehensively discuss their influence, if any, on TBC longevity. The improved understanding of the rather complex pore size distribution in ASPS TBCs, and their individual influence on thermo-mechanical properties as well as longevity of the coatings, emerging from this study has important design implications and can facilitate tailoring of highly durable ASPS sprayed columnar microstructures with optimum functional performance.

2. Experimental methods and characterization

2.1. Coating materials and deposition techniques

The substrate, bond coat and top coat materials used in this work were Hastelloy®X, commercial CoNiCrAlY powder (AMDRY 9951, Oerlikon Metco, Wohlen, Switzerland) and commercial suspension of 8 wt% yttria stabilized zirconia (8YSZ) (INNOVNANO, Coimbra, Portugal), respectively. The suspension used had a particle size distribution of d10 = 100 nm, d50 = 500 nm and d90 = 1 μm and a solid load of 25 wt% 8YSZ in ethanol. All the substrates were first grit blasted with Alumina powder (220 grit) prior to bond coat deposition. A bond coat of 200 μm ± 15 μm thickness was then deposited using a M3™ supersonic high velocity air fuel (HVAF) spray gun (Uniquecoat, Richmond, USA) with spray parameters developed in previous works [16,18,19]. Finally, the top YSZ layer of about 250–300 μm was deposited using an Axial III high power plasma torch (Northwest Mettech Corp., Vancouver, Canada) equipped with a Nanofeed 350 suspension feed system.

Four discrete sets of process parameters were used for YSZ layer deposition on identically bond coated substrates. It is pertinent to indicate that the authors' group has been working on TBCs deposited with the above suspension and spraying technique for the past 4 years [18,19]. Hence, the specific intent of the present study was to use discrete parameter sets (provided in Table 1) modified from previous works [18,19] to yield different columnar-type structures and determine how the thermal shock life is influenced by the microstructural variations, especially in terms of different length scaled pores or pore size distribution and total porosity. Table 1 also shows the thickness for all coatings along with their respective deposition rate.

The specimens coated were of two different geometries: thin square plates (25 mm × 25 mm × 1.6 mm) and thick coupons (ϕ 25 mm × 6 mm). The thick coupons were subjected to cyclic thermal shock test whereas the thin plates were used for determining the microstructure, thermal diffusivity and mechanical properties.

Table 1
Discrete sets of plasma spray parameters utilized to deposit different columnar YSZ layers with their corresponding thickness and deposition rate.

Coating #	Spray distance (mm)	Suspension feed (mL/min)	Total gas flow (L/min)	Power (kW)	Enthalpy (kJ)	Coating thickness (μm)	Deposition rate (μm/pass)
1	100	45	200	110	9.9	268 ± 21	1.1 ± 0.1
2	100	45	300	108	7	273 ± 24	1.4 ± 0.1
3	75	70	250	119	11.1	248 ± 16	3.3 ± 0.2
4	75	100	300	142	12.4	305 ± 18	7.6 ± 0.4

2.2. Thermal shock testing

Thermal shock testing of all the samples was performed in a propane gas combustion burner rig facility at GKN Aerospace (Trollhättan, Sweden) [29]. The samples were subjected to thermal cycling, with each cycle involving 75 s of heating followed by 75 s of cooling. The test started with initial preheating of the sample from behind the substrate side using hot air guns to a temperature of about 700 °C. Samples were then heated from the front ceramic top coated side to a maximum temperature of about 1300 °C. Accordingly, the ceramic coating experiences a temperature gradient, which may vary depending on the thermal properties of each coating. After the 75 s heating period, the front face of the sample (ceramic top coat) was cooled using compressed air for 75 s. The front face of the samples was found to attain a temperature of around 300 °C by the end of the cooling period. The integrity of each sample surface in terms of visible cracking, spallation etc. was automatically captured by a video camera and both the front and back surface temperatures were monitored using pyrometers. The failure criterion was 10% spallation of the coated surface as observed during the video recording and the number of cycles to spallation was noted as the thermal shock lifetime of the sample. Six samples were subjected to thermal shock testing per coating in order to get a statistical deviation.

2.3. Isothermal heat treatment

The thin square plate samples were first water jet cut into ϕ10 mm small coupons which were then subjected to isothermal heat treatment. Samples were placed in a furnace at room temperature, the furnace was then evacuated and flushed with a Argon-2.9 Vol% Hydrogen mixture maintaining a flow rate of 200 L/h and heated to a temperature of 1100 °C in about 4 h. Four sets of samples were held at this temperature for 1, 3, 10 and 200 h respectively. At the end of the test, the samples were cooled down to room temperature in about 4 h.

2.4. Microstructure analysis

The microstructure of both metallographically prepared (polished) and fractured surfaces were analyzed by scanning electron microscopy (SEM) using HITACHI TM3000 (Tokyo, Japan), MIRA3 FEG (TESCAN, Brno, Czech Republic) and EVO 50 (ZEISS, Oberkochen, Germany) microscopes. For examining fractured cross-section microstructures, the top coat was first detached from the substrate by immersing the coated specimens in aqua-regia (a mixture of concentrated HCl and HNO_3 in molar ratio 3:1). The detached ceramic top coats were then cleaned with ethanol, dried and broken manually in several pieces. In addition, the surface of each coated sample was also rapidly milled in such a way that only about several micrometers of the top ceramic layer was removed/broken to enable observation of the 'fractured' topography. Prior to analysis of polished cross-sections, the samples were mounted using vacuum impregnation in a low viscosity epoxy resin and then cut using an Aluminum oxide cut-off wheel. The transverse sections were again cold mounted using a fast curing epoxy resin. The double mounted samples were then ground and mirror polished semi-automatically using a Buehler PowerPro 5000 (Buehler, USA), polishing machine.

2.5. Porosity analysis

Porosity measurement is a challenge in SPS sprayed coatings due to the inherent wide pore size distribution (ranging in scale from -μm to -nm sized pores) [18,19]. In order to measure the entire range of porosity, two different techniques were used. Previous work has shown that image analysis and mercury infiltration porosimetry (MIP) can be suitable techniques for porosity measurement in SPS coatings. It was shown that the Image analysis technique can be unreliable while measuring the fine porosity (sub-micron and, especially, nano-sized) and may, therefore, under predict the porosity [18,19]. Other techniques as reported in literature for measuring fine porosity are Brunauer–Emmett–Teller (BET) and MIP, where BET is reported to be useful while measuring porosity between 2 nm to 300 nm [30] whereas MIP is reported to be useful for a wider range i.e. from few nm to few tens of μm [19]. Although MIP has shown a pore size resolution of down to a few nm [18,19] and capable for measuring wider pore size range, the larger pores measured by MIP in the low pressure regime can be significantly influenced by the surface roughness of the coating [18,19]. Hence, a combination image analysis and MIP techniques, as described below in detail, was used to analyze the total porosity. The porosity was categorized in four different classes based on pore size (diameter): Class-1 (>10 μm), Class-2 (10 μm–1 μm), Class-3 (1 μm-100 nm) and Class-4 (<100 nm). The classification of pores as mentioned above was selected in order to differentiate the large (>10 μm), micron (1 μm–10 μm), sub-micron (1 μm-100 nm) and nano (<100 nm) sized pores and study their individual role on coatings performance. The Class-1 and Class-2 pores were analyzed by image analysis while Class-3 and Class-4 pores were determined by MIP.

2.5.1. Image analysis

Class-1 and Class-2 porosity was analyzed using the ImageJ software, a public domain java based image processing program (Fiji (Fiji Is Just ImageJ)) [31]. At a magnification of ×500, 30 micrographs were captured using SEM at various locations in the cross-section of the polished specimen to determine the representative value of the porosity. Fig. 1 (a–e) depict the procedure used for classifying the Class-1 and Class-2 porosity. As can be seen from Fig.1, the SEM image at ×500 (a) was first cropped appropriately to obtain (b), and the auto-brightness contrast adjustment used to automatically threshold and convert the micrograph into a binary image (c). A count mask was then used to delineate the desired size ranges, i.e., >10 μm for Class-1 (d) and 1 μm–10 μm for Class-2 (e) [32]. The porosity percentage for each class was then calculated from the respective binary images as an area fraction of the white region (the remaining pores after the relevant count mask was applied) with respect to the total area. The procedure was automated for all the images and the mean value of % porosity was determined for each class. Fig. 1 (f–i) also illustrates a similar procedure that could, in principle, also be adopted for counting Class-3 (h) and Class-4 (i) pores using a high magnification (×7000) SEM micrograph (f) and its corresponding binary image (g). However, these pores (Class-3 and Class-4) were not counted using image analysis as it is amply evident that such a procedure could under-predict the fine porosity.

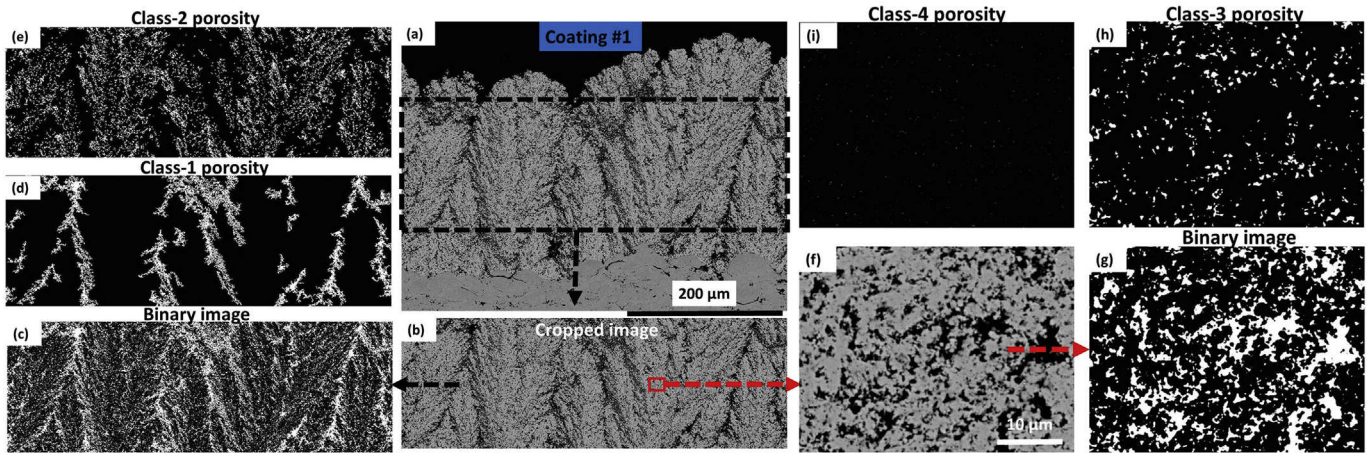

Fig. 1. Image analysis procedure, also showing the four defined classes of porosity: Class-1 (>10 μm), Class-2 (10 μm–1 μm), Class-3 (1 μm–100 nm) and Class-4 (<100 nm) in (d), (e), (h) and (i) respectively.

2.5.2. Mercury infiltration porosimetry (MIP)

A rectangular specimen (10 mm × 20 mm) was water jet cut from a thin coated square plate which was then kept in aqua-regia in order to detach the ceramic top coat from the substrate. The free-standing ceramic top coat was then used for MIP measurements. The porosity was measured using a PASCAL 440 system (POROTEC GmbH, Germany), which had a detection limit down to a pore diameter of 3.6 nm [33]. The raw data was extracted and only Class-3 and Class-4 pores were considered. A detailed description of the MIP technique used can be found elsewhere [33,34].

Total porosity in each coating was then determined by summing up the porosity in the 4 different pore-size ranges (Class-1 to Class-4) measured by the techniques mentioned above.

2.6. Column density measurement

To measure the column density, a number of SEM images were taken at a magnification of 200× over the entire cross-section of the coating. A straight line was drawn at half of the coating thickness and the length of the resulting line was measured in micrometers. All the column boundaries, intersecting the line and having a length greater than half of the coating thickness were counted. The column density (columns/mm) was then calculated, using eq. (1) [18]:

$$column\ density = \frac{(No.of\ column\ boundaries\ intersecting\ the\ line - 1)}{True\ length\ of\ the\ line} \quad (1)$$

2.7. Phase analysis

The phase constitution of coatings in the as-sprayed state and after thermal shock testing was determined by X-ray diffraction (XRD) using an X-ray Power D8 Discover diffractometer (Bruker AXS, Germany) with Cu-Kα radiation in the 20 to 90° 2θ range. Refinement of lattice parameters as well as quantification of the identified phases and the mean crystallite size was done using TOPAS 4.2 software.

2.8. Thermal conductivity

The thermal conductivity of a TBC is derived from its thermal diffusivity. The relation between coating's thermal conductivity (λ), thermal diffusivity (α), specific heat capacity (C_p) and density (ρ) is shown in Eq. (2), where all symbols are in SI units:

$$\lambda = \alpha C_p \rho \quad (2)$$

The coating density was derived from its bulk density (6.1 g/cm^3 for 8YSZ) and the total porosity measured using the combination of methods described above. The specific heat capacity was measured in earlier work [9] by differential scanning calorimeter 404C (Netzsch Gerätebau GmbH, Selb, Germany) [9] while for thermal diffusivity measurements laser flash analysis (LFA) was employed using LFA 427 (Netzsch Gerätebau GmbH, Germany) equipment [19,35].

2.9. Mechanical properties

Hardness and E-modulus were experimentally determined using an instrumented depth-sensing micro-indentation technique. A computer controlled micro-indenter equipment (H100, Fischerscope, Helmut Fischer GmbH, Germany), having an indenter displacement resolution in the nanometer range and a load resolution of 0.4 mN during the entire loading and unloading duration, was used. Instrumented hardness (H_{IT}) (convertible into Vickers' hardness scale HV) and instrumented E-modulus (E_{IT}) (obtained from the unloading slope) were determined using the commercial WIN-HCU® software (Fischer GmbH) using Eqs. (3) and (4):

$$H_{IT}(MPa) = \frac{P}{A_i} = \frac{P}{Constant \times h^2} \quad (3)$$

$$E_{IT}(GPa) = \frac{E}{(1-\nu^2)} = \frac{P \times \pi^{0.3}}{4\ tan68^\circ\ h\ (dH_{IT}/dP)P_{max}} \quad (4)$$

where P is the indentation load in (N), A_i is the indented area, h is the indentation depth, *Constant* is the ratio of the indented area to the square of the indentation depth (since the ratio is constant for a given indenter), E is the E-modulus of the coating in (GPa), ν is the Poisson's ratio for 8YSZ, which was considered as 0.25 [1] and P_{max} is the maximum load used during indentation. A total of 25 indents were made on as-sprayed polished cross-sections with a maximum load of 1 N (HV0.1) and the average values of both hardness and E-modulus, were determined [1].

Fracture toughness measurements were made using the Vickers indentation technique. Prior to toughness measurements, all the coatings were first mirror polished and then indented at a maximum load of 9.807 N (HV1), which was identified as optimum for such coatings to produce Palmqvist type cracks without significantly damaging the coating, for a dwell time of 13 s [36] using a Vickers indenter (Shimadzu HMV-2 T Microhardness Tester). A total of 25 indents were made all

across the mirror polished cross-section. SEM images for all the indents were captured in order to measure the crack length (l) and the indent half-diagonal length (a). The following equation was used to calculate the fracture toughness, as the cracking pattern was identified as Palmqvist cracks ($0.25 \le l/a \le 2.5$) type in these coatings [37]:

$$K_{IC} = 0.018 \left(\frac{E}{H_{IT}}\right)^{\frac{2}{5}} H_{IT} a^{\frac{1}{2}} \left(\frac{a}{l}\right)^{\frac{1}{2}} \quad (5)$$

Here K_{IC} is the mode I indentation fracture toughness ($MPa.m^{1/2}$), E is the elastic modulus (MPa) determined from E_{IT}, a is the indentation half-diagonal length (m) and l is the crack length (m). Average values of E, H_{IT}, a and l were considered in order to calculate the mean K_{IC} and the values are reported with appropriate standard deviations calculated using the law of error propagation. All the indents were made at a depth that was about half of the coating thickness and approximately in the center of the columns. It is important to emphasize that all the indents were made at approximately the center of the YSZ columns for the sake of reliable measurements. Thus, the determined K_{IC} values provide only the local toughness and can be considered to be the upper bounds of effective toughness in coatings investigated.

3. Results

3.1. As-sprayed columnar microstructures

Four different columnar coatings were produced using discrete process parameters provided in Table 1. The resultant SEM micrographs of the polished cross-sections of these columnar microstructures are shown in Fig. 2. It is amply evident that the microstructures in the four samples, although columnar, are quite distinct in character. The nature of the columns, the pore size as well as the extent of porosity present within each column and at/near the inter-columnar region are clearly seen to be different in each of the coatings. Attention can also be drawn to the presence of inter-pass porosity bands (shown in Fig. 2 (d) by white dotted arrows) that were exclusively observed in Coating #4 and not in any other coatings. A closer examination of the topography of these coatings as well as their polished and fractured cross-sections at both low and high magnification, particularly within the columns and close to the column gaps, was employed to evaluate the differences. This was meticulously done in case of all the coatings.

Various polished and fractured SEM micrographs at different magnifications as shown in Fig. 3 and Fig. 4 reveal the different regions of interest in the TBCs studied, although they have been illustrated here for Coating #1 and Coating #2, respectively. Fig. 3 shows high magnification micrographs of the polished cross-section of the same coating depicted in Fig. 2 (a), providing closer views of a region within column (Fig. 3(a)) as well as of a region in the vicinity of an inter-columnar spacing (Fig. 3 (b). The top view as well as the cross-section of the fractured coating is shown in Fig. 4(a) and Fig. 4(b), respectively. Further magnified micrographs of regions within the fractured column and within the fractured inter-columnar spacing are also shown in Fig. 4 (c) and Fig. 4(d), respectively.

The extent to which all the features indicated in Figs. 3 and 4 are present in a given coating is governed by their respective spray parameters. These also lead to expected differences in individual contributions of different pore classes (Class-1 to Class-4) to the overall porosity content in the TBC specimens as quantified below.

3.2. Quantification of porosity and pore size distribution in as-sprayed coatings

The four different classes of porosity, i.e. Class-1 (>10 μm), Class-2 (10 μm–1 μm), Class-3 (1 μm–100 nm) and Class-4 (<100 nm), were quantified as described in Section 2.5 through a combination of image

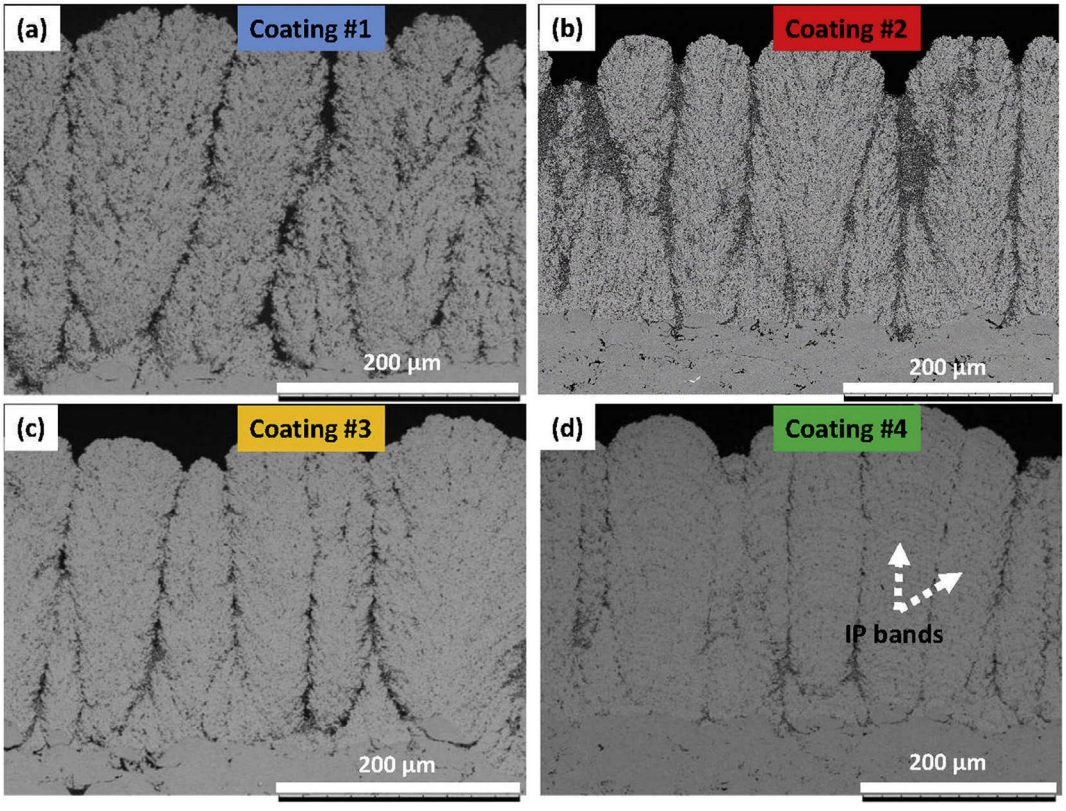

Fig. 2. The polished cross–sections of all coatings showing columnar structures (a to d for Coating #1 to Coating #4, respectively) with distinct microstructures (note the white dotted arrows in (d) which depict inter-pass porosity (IP) bands observed only in Coating #4).

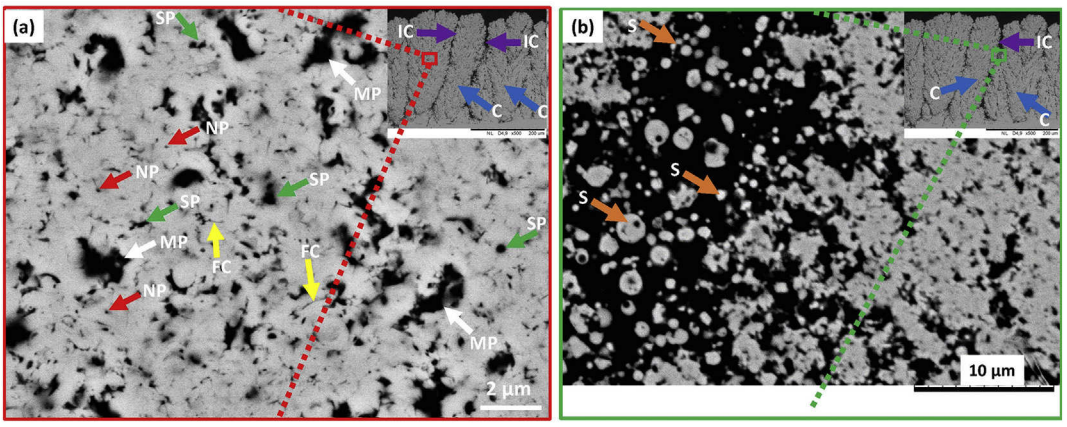

Fig. 3. Magnified polished cross-section micrograph within the column (a) and within the inter-columnar spacing (b) for Coating #1 showing various microstructural features marked with different colored arrows and notations, namely columns (C in blue), inter-columnar spacing (IC in violet), spherical particles (S in orange), fine cracks (FC in yellow), nano pores (NP in red), submicron pores (SP in green) and micron-sized pores (MP in white).

analysis and MIP. The results are summarized for as-sprayed coatings in Fig. 5(a) and also utilized to determine the total porosity in each coating after summing up the contribution of all four porosity classes. It can be seen from Fig. 5(a) that Coating #1 has the highest total porosity (about 45%) followed by Coating #2 (about 33%), Coating #3 (about 26%) and Coating #4 (about 16%). It is also educative to determine the average contribution of each class of porosity of all four coatings to the total porosity which is plotted in a pie-chart as shown in Fig. 5(b). It can be noticed from Fig. 5(b) that the Class-3 pores were the most dominant in a majority of the coatings (40%), followed by Class-2 (34%). Class-4 pores were found to contribute the least among all classes (7%) to the total porosity in case of all the coatings.

3.3. Change in porosity upon isothermal heat treatment

Two extreme coatings in terms of total porosity content in the as-sprayed condition (Coating #1 and Coating #4) were also analyzed after 200 h of isothermal heat treatment in an inert atmosphere and the porosity results are summarized in Fig. 6. The porosity in Coating #1 and Coating #4 after 200 h was found to have marginally changed

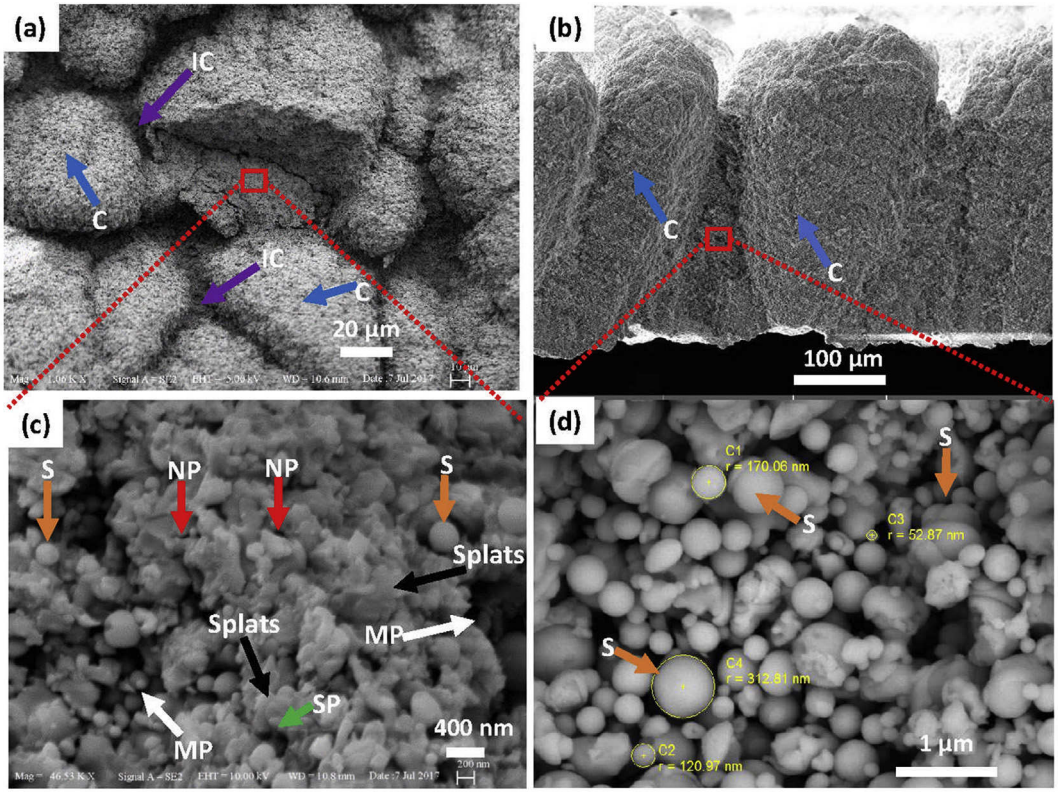

Fig. 4. Different fractured micrographs showing top view of a fractured column (a), a fractured cross-section (b), a magnified fractured micrograph within the column (c), and within the inter-columnar spacing (d) of Coating #2 and also various features, namely columns (C in blue), inter-columnar spacing (IC in violet), well-molten splats (in black), spherical particles (S in orange), nano pores (NP in red), submicron pores (SP in green) and micron pores (MP in white).

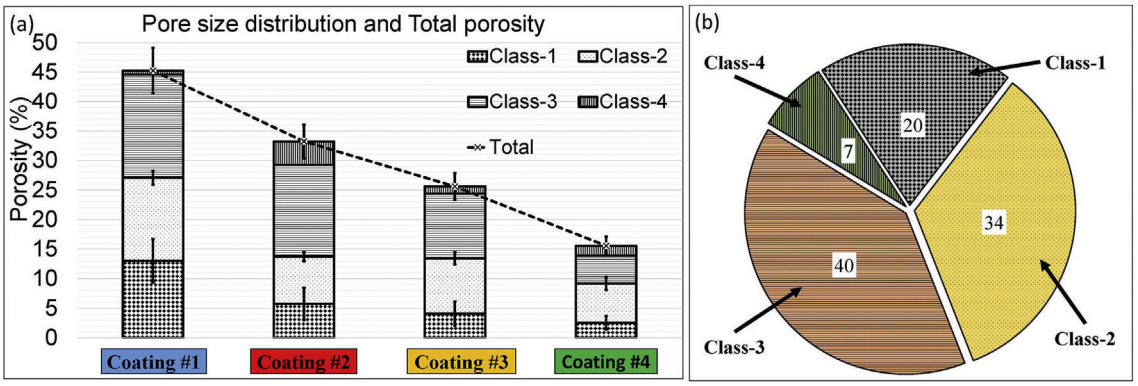

Fig. 5. Total porosity content and absolute contribution of each class of porosity for the four different coatings (a) and % share of each pore class to the total porosity averaged over the four coatings (b).

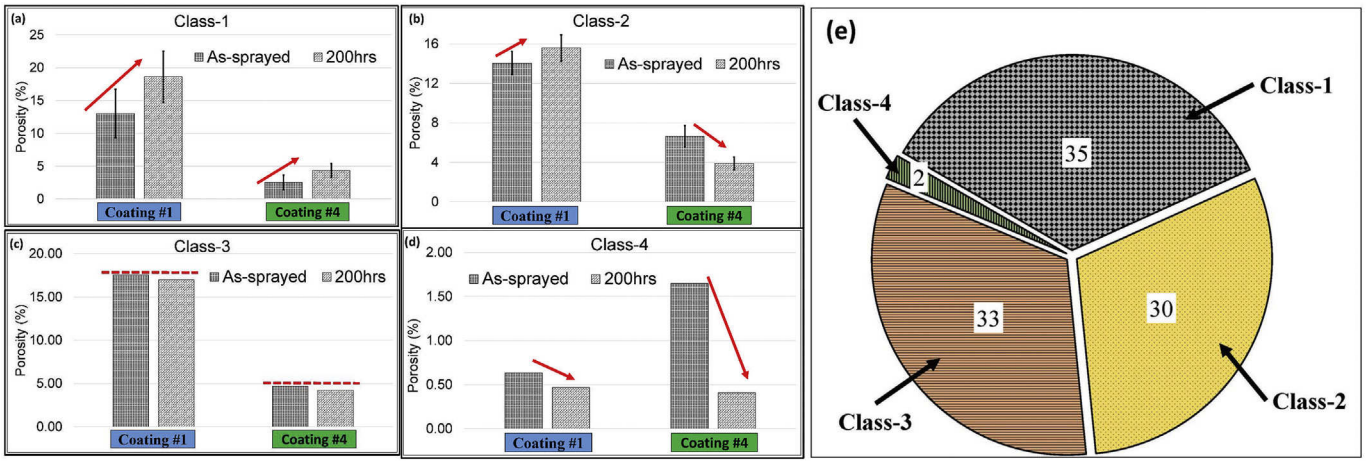

Fig. 6. Change in different classes of porosity for Coating #1 and Coating #4 after isothermal heat treatment for 200 h in an inert atmosphere (a-d) and % share of each pore class to the total porosity averaged over the four coatings after heat treatment (e).

from (45% ± 4%) to (52% ± 4%) and (16% ± 2%) to (13% ± 1%), respectively. However, careful inspection of different classes of porosity revealed that pores of different length scales responded differently when subjected to heat treatment, as shown in Fig. 6. For instance, the Class-1 porosity was found to increase while Class-4 porosity was found to decrease in both coatings. Class-2 porosity showed a mixed behavior, with increase in case of Coating #1 and decrease in case of Coating #4 being noted, whereas the amount of Class-3 pores present was found to be virtually unaffected. The average contribution of each class of porosity of both coatings to the total porosity after heat treatment is also plotted in a pie-chart as shown in Fig. 6(e). It can be noted that the contribution of Class-4 porosity, like in as-sprayed state, is still the least among all classes, in fact negligible (only 2%), whereas other porosity classes were found to contribute in a similar range of about 30–35% each. It is also important to note from Fig. 5(b) and Fig. 6(e), a significant change (15% increase) in an average Class-1 porosity content in such columnar coatings after the heat treatment occurred.

3.4. Phase analysis by XRD

XRD analysis performed on both the as-sprayed as well as failed (after thermal shock testing) samples showed that there was no phase transformation in any of the four coatings. The lattice parameter ratio ($\sqrt{2}(c/a)$) calculated for all coatings before and after failure was found to be lower than 1.010, confirming that the non-transformable tetragonal (t′) phase was retained even after failure [38]. This suggests that the failure in these coatings was not attributable to phase transformation, which can potentially contribute to failure in 8YSZ coatings at higher temperatures [39]. Similar observations were also made for samples after the isothermal heat treatment, with no phase change in coatings being noticed.

3.5. Thermal shock lifetime

The performance of all four TBCs under thermal shock testing was determined in terms of number of cycles to failure as defined in Section 2.2 and is summarized in Table 2. It can be noted that the thermal shock life of Coating #1 was the lowest (about 100 cycles) while the Coating #4 one the highest (about 500 cycles). In fact, the lifetime of Coating #4 was exceptionally higher compared to the rest. It is pertinent to mention here that the lifetime in excess of 1000 cycles have been reported in case of both the standard APS TBCs [12] as well as ASPS TBCs [16] having a thickness similar to that of the coatings studied in this

Table 2
Thermo-mechanical properties (thermal conductivity, Vickers hardness, indentation E-modulus and mode I fracture toughness) of as-sprayed coatings and their thermal shock lifetimes.

Coating #	Thermal conductivity (W/m·K)	Vickers Hardness (HV0.1)	Indentation E-modulus (GPa)	Fracture toughness ($MPa \cdot m^{0.5}$)	Lifetime (No. of cycles to failure)
1	0.53 ± 0.01	454 ± 48	63 ± 8	1.39 ± 0.02	102 ± 17
2	0.73 ± 0.01	630 ± 96	72 ± 6	1.58 ± 0.03	138 ± 32
3	1.20 ± 0.02	782 ± 57	106 ± 5	1.72 ± 0.03	228 ± 54
4	1.39 ± 0.03	945 ± 87	94 ± 6	1.73 ± 0.03	529 ± 128

work. This lends further credence to the importance of tailoring ASPS microstructures for achieving optimum TBC durability as attempted herein, since mere realization of a columnar microstructure clearly does not guarantee high lifetime.

3.6. Thermo-mechanical properties

As shown in Table 2, the thermal conductivity was found to be least for Coating #1 (0.53 W/mK) and the highest for Coating #4 (1.39 W/mK). Low thermal conductivity is a crucial requirement for a TBC to impart the necessary thermal insulation required by gas turbine components during operation. The highest thermal conductivity measured in case of Coating #4 is still lower than the typically reported values for EBPVD TBCs, which are about 1.5–1.9 W/mK [22,40]. Also, the lowest thermal conductivity (observed in Coating #1) is lower than the typically reported values for traditional APS TBCs which are about 0.7–1.1 W/mK [9,41]. Similarly the mechanical properties such as hardness, fracture toughness and modulus of elasticity of as-sprayed coatings are also summarized in Table 2. It can be noticed that both hardness and toughness were the least for Coating #1 and the highest for Coating #4, suggesting a direct correlation with total porosity in the coating. In case of E-modulus, no such correlation was apparent, with Coating #1 showing the lowest value followed by Coating #2, Coating #4 and Coating #3 in that order.

4. Discussion

4.1. Influence of process parameters on coating microstructure

As explained in the introduction, the coating build-up in SPS and the resultant microstructure are mainly governed by the suspension properties as well as the plasma spray parameters. Since the same suspension was used to deposit all four coatings, any variation in microstructures can be attributed exclusively to differences in plasma spray parameters.

The extent of suspension fragmentation in the plasma (viz. droplet size) in combination with its velocity govern the droplet momentum which, in turn, governs column formation (lower droplet momentum favors columnar microstructures) and coating build-up [14,15,42]. Since all coatings revealed a columnar structure (see Fig. 2(a to d)), the extent of suspension fragmentation was adequate to produce fine droplets that exhibit low momentum necessary for column formation [14,15]. However, the column density, as can be seen from Fig. 7, was significantly different in the four coatings and this can be attributed to the different spray conditions.

Lower suspension feed rate, higher total gas flow rate and higher power can augment suspension fragmentation and, hence, reduce droplet size. Also, a longer spray distance implies that the droplets/particles reaching the substrate may have a lower velocity compared to those which travel a shorter spray distance (provided other parameters are identical). Lower droplet momentum can be achieved by having either finer droplets or slower droplet/particle velocity or both. This can explain the difference in column density shown in Fig. 7.

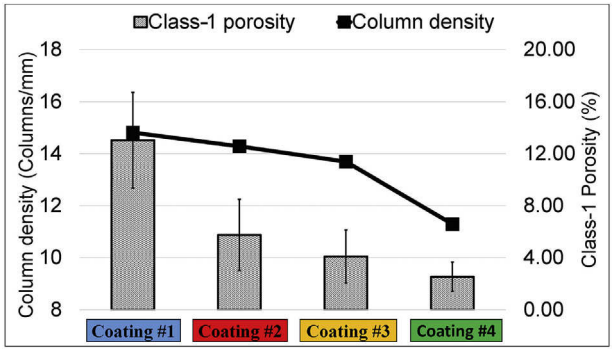

Fig. 7. Column density and Class-1 porosity for all four coatings and the relationship between them.

More columns in the microstructure also result in more inter-columnar spacing. As can be seen from Fig. 1, the Class-1 porosity is largely attributable to the region at/near the inter-columnar spacing in the columnar microstructure. The dependence of Class-1 porosity on column density can also be seen from Fig. 7. However, it should also be appreciated that, apart from column density, the width of the inter-columnar spacing and the connected spread of pores in its immediate vicinity also contribute to the Class-1 porosity (see Fig. 1(d)).

After solvent evaporation from the droplet, the YSZ particles are directly exposed to the plasma. The degree of melting of these particles and formation of a well-molten splat upon their impact with the bond coat depends on adequate dwell time in the plasma plume as well as plasma energy being available. The dwell time can be governed by several spray parameters such as spray distance, suspension feed rate and total gas flow, while the plasma power and enthalpy are good indicators of the available energy. Shrinkage of these well-molten splats during solidification may introduce some fine inter-splat cracks/porosity in the microstructure as can be seen in Fig. 3(a) and Fig. 4(c) and can contribute to Class-3 and/or Class-4 porosity. For example, the extremely high power and enthalpy used to deposit Coating #4 were adequate to melt the particles, despite the high suspension feed rate and short spray distance, to achieve proper splats. This led to the lowest total porosity in Coating #4 compared to all other coatings.

If the YSZ particles are not fully molten in flight, they can result in formation of μm-sized pores marked in Fig. 3(a) and Fig. 4(c), contributing to either Class-2 or Class-3 porosity. Moreover, in a situation when lower power and enthalpy is used in combination with a significantly high spray distance, the molten YSZ particles may even re-solidify before reaching the substrate resulting in spherical particles instead of splats as shown in Fig. 3(b), Fig. 4(c) and Fig. 4(d). They can result in the formation of fine pores (submicron or nm-sized pores, depending on their size which was found to be around 50 nm–300 nm as shown in Fig. 4(d)) marked in Fig. 3(a) and Fig. 4(c), contributing to either Class-3 or Class-4 porosity. All this is clearly evident in the microstructures of Coating #1 and Coating #2, which were sprayed at lower power and enthalpy.

Apart from the different sized pores/cracks, it is also pertinent to discuss the presence of inter-pass (IP) porosity bands marked with white dotted arrows in Fig. 2(d). As mentioned earlier, these were found only in case of Coating #4, which may be due to the relatively higher rate of material deposition per pass in Coating #4 than other coatings. As can be seen from Table 1, the deposition rate for Coating #4 was more than twice the Coating #3 and about seven times higher than that of Coating #1. Few unmolten particles are inadvertently generated along the periphery of the plasma jet, along with the fully molten splats. During the repeated passage of the plasma torch corresponding to the number of passes, these undesired particles may get deposited above and below the desired molten splats resulting in such porosity bands. Such porosity bands can be distinctly visible especially when high material deposition rate per pass is used as in case of Coating #4. These porosity bands were found to be contributing to either Class-2 and or Class-3 porosity.

4.2. Influence of microstructure on thermal shock lifetime

The photographs of all the four failed coatings shown in Fig. 8(a-1 to a-4) revealed that the coatings did not spall at the edges as in case of TCF tests, where typical failure has been reported to initiate at the edges [43,44]. All the coatings were seen to be chipped off from the center of the ceramic top coat. Similar failure mode was reported for ASPS deposited TBCs by Zhou et al. [45] tested during thermal shock in a different

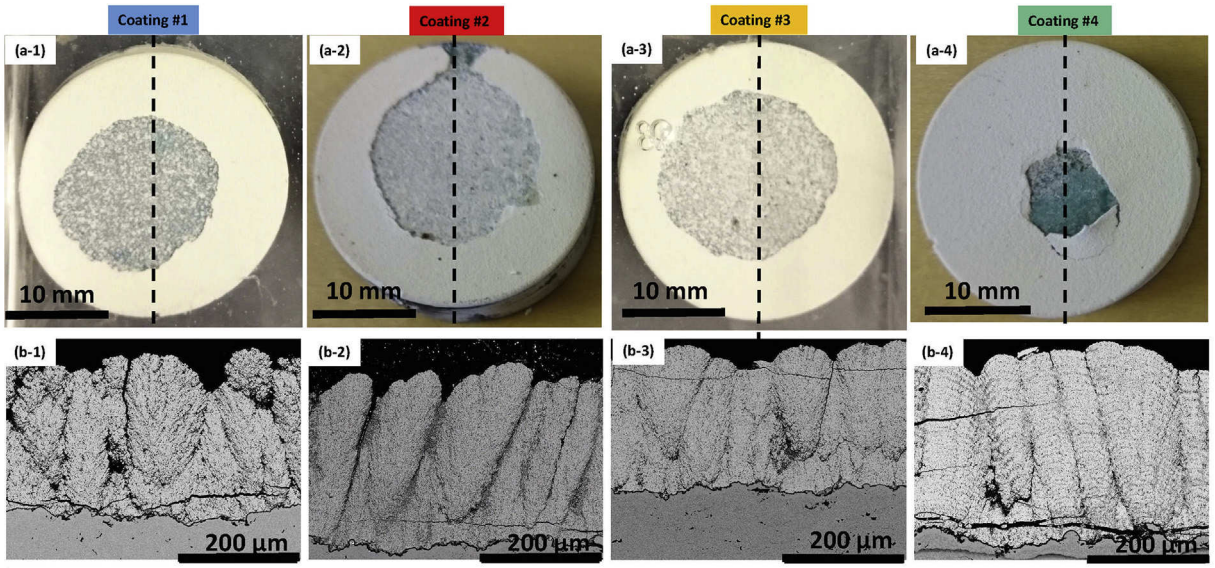

Fig. 8. Photographs of all coatings after failure (a-1 to a-4) and the corresponding SEM cross-section micrographs (b-1 to b-4) along the dotted lines for Coating #1 to Coating #4.

burner rig test facility. In addition, the SEM micrographs of all the failed coatings revealed the presence of horizontal cracks in the YSZ layer, suggesting that the propagation of such cracks could have ultimately led to delamination of the top coat. Moreover, these horizontal cracks are typically observed in the YSZ layer close to the bond coat. The SEM micrographs of all the failed coatings also confirmed that the TGO thickness was too small to be the predominant cause of failure. For example, magnified micrographs of the bond coat-top coat interface for Coating #2 (Fig. 13(b-1)) clearly show the thickness of the TGO to be about 2–3 µm and similar observations were also made for all other coatings as well. Although the TGO thickness at failure has been reported to be above 5–6 µm in case of APS TBCs subjected to TCF tests [6], it is relevant to mention that a similar TGO thickness of 2–3 µm has also been noted in case of prior studies after thermal shock testing of ASPS TBCs [45]. Therefore, the failure in the present case can be mainly attributed to crack initiation and propagation in the ceramic top coat and not the TGO as reported in furnace TCF tests or other thermal shock gas burner tests [43].

From the standpoint of eventually developing an ability to tailor SPS TBC coating microstructures to enhance thermal shock performance, it is important to understand the role of various factors in governing TBC lifetime, as is well-known today in case of APS TBCs. As a first step in investigating the life-determining attributes of ASPS TBCs exposed to thermal shock, due to the relatively complex microstructure of SPS, this involves correlating the total porosity in as-deposited coatings (as well as the distribution of different previously defined pore classes) to their longevity. The thermal shock lifetime of the four coatings investigated was plotted against total porosity in Fig. 9. The total porosity was seen to have a strong influence on the lifetime of ASPS TBCs and, for the range of porosity studied in this work (15%–45%), the lifetime progressively decreased with increase in total porosity. Similar to the total porosity, the lifetime in this study has also showed a decreasing trend with both the porosity at/near the inter-columnar spacing (Class-1) as well as within the column Class-(2 + 3 + 4) as shown in Fig. 9. This suggests that along with the total porosity, different porosity classes can also play a significant role on lifetime which is discussed in more details in later sections. It is, however, to be appreciated that the influence of porosity on coating durability is indirect in nature and in actual fact a consequence of the effect that porosity has on the thermo-physical properties of the TBCs. Hence, it is important to first identify the various thermo-physical properties that significantly affect TBC lifetime, so that the microstructure can be tailored to appropriately manipulate those properties.

4.3. Influence of thermo-physical properties on thermal shock lifetime

It has been proposed in the past that the lifetime of ceramics subjected to thermal shock can be analyzed by analyzing their thermal shock resistance [46–48]. Kingery and Hasselman introduced various thermo-physical properties of ceramics which should be considered for evaluating their thermal shock resistance such as thermal conductivity, modulus of elasticity, coefficient of thermal expansion, fracture strength, heat transfer coefficient, specimen size etc. [46,47]. Lu et al. [48] derived a relationship between thermal shock resistance and the above properties for various cases, including engineering ceramics containing a dominant through thickness flaw with low biot number ($Bi < 1$) and proposed that the thermal shock resistance (ΔT) in such a case is proportional to the ratio between a product of fracture toughness (K_{IC}) and thermal conductivity (λ) and a product of modulus of elasticity (E), thermal expansion coefficient (α), heat transfer coefficient (h) and thickness (H). The original expression by Lu et al. is shown below in Eq. (6) [48].

$$\Delta T \equiv Constant * \frac{\lambda K_{IC}}{E \alpha \sqrt{\pi H}\, hH} \tag{6}$$

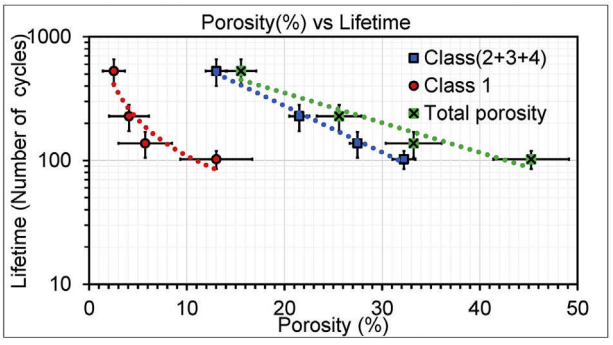

Fig. 9. Dependence of TBC lifetime on as-sprayed total porosity, Class-1 porosity and Class-(2 + 3 + 4) porosity.

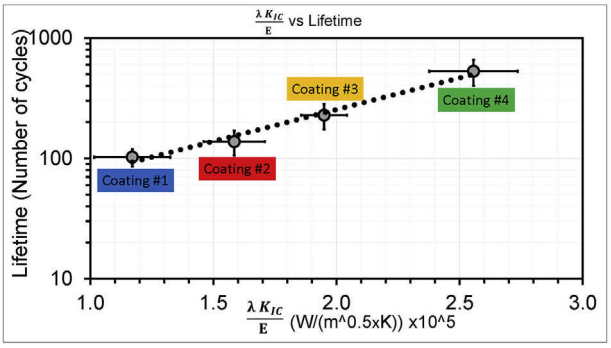

Fig. 10. Relationship between lifetime and ($\frac{\lambda K_{IC}}{E}$) for all coatings.

It is educative to discuss the above equation in the context of the thermal shock performance of the ASPS coatings which exhibit through thickness "flaws" in the form of inter-columnar spaces and also possess a low Biot number ($Bi \approx 0.94$, assuming heat transfer coefficient to be 5000 $W/m^2 \cdot K$ [49] for 8YSZ coating). The thermal expansion coefficient, heat transfer coefficient and thickness can be deemed to be constant in the present discussion, since the coating material was identical and the thicknesses similar in all four TBC specimens studied herein. Therefore, as per Eq. (6), it seems informative to study the relationship between the thermal shock lifetime and the ratio of the product of conductivity and toughness and E-modulus ($\frac{\lambda K_{IC}}{E}$). The dependence is illustrated in Fig. 10, which clearly suggested that, there exists a good correlation between the ratio ($\frac{\lambda K_{IC}}{E}$) and the thermal shock lifetime. For this reason, it is deemed educative to consider the manner in which these three properties, namely conductivity, E-modulus and toughness, can possibly impact TBC durability.

4.3.1. Thermal conductivity

As reported in published literature, the TBCs experience a much more severe thermal gradient across the ceramic top coat layer during thermal shock testing compared to isothermal TCF testing [50]. A higher thermal gradient across the ceramic top coat layer can affect the bond coat temperature (which, in turn, can affect TGO formation) as well as the thermal mismatch stresses in the ceramic top coat (especially near the bond coat – top coat interface), thereby affecting the lifetime [51]. The thermal gradient is, of course, significantly dependent on the thermal conductivity of the coating. A higher thermal conductivity of the ceramic top coat lowers the temperature drop across it and leads to the bond coat experiencing higher temperatures which, as reported by Vassen et al., can result in lower lifetime due to corresponding accelerated TGO growth and increase in thermal expansion mismatch stresses [43]. Thus, unlike in bulk ceramics, it is inappropriate to consider the influence of thermal conductivity on the 'thermal shock resistance' of the ceramic layer alone in case of the comparatively complex TBC systems, wherein the role of thermal conductivity on changes to the underlying bond coat is inseparable in governing TBC longevity. Moreover, low thermal conductivity is a major functional requirement of the TBCs and, hence, increasing the thermal conductivity to enhance its thermal shock resistance as suggested by Eq. (6) is not an implementable option.

4.3.2. E-modulus and toughness

Both E-modulus and toughness in TBCs are altered with time during high temperature exposure due to associated microstructural changes, such as sintering of ceramic top coat [52]. Since all the coatings were exposed to high temperature during thermal shock testing for several hours (the actual number of hours before failure for all the coatings in this study were approximately between 2 and 13 h), the effect of an average E-modulus and toughness (determined in as-sprayed condition, and after 1, 3 and 10 h of isothermal heat treatment) on TBC lifetime has been plotted in Fig. 11. It can be seen from Fig. 11(a) that the TBC lifetime increases with increase in E-modulus.

The toughness also has a significant influence on TBC lifetime as shown in Fig. 11(b), with the thermal shock life increasing with the increase in toughness. It should be borne in mind that E-modulus and toughness are interrelated. As can be seen from Fig. 11(c), there exists a good correlation between toughness and E-modulus, which has also been observed in conventional APS TBCs [52]. Therefore, both Eq. 5 and Fig. 11(c), suggest that the coating toughness in some respect "incorporates" the E-modulus. Consequently, it is appropriate to consider the toughness of the ceramic top coat to be the most dominant life-determining factor. Such a direct relationship between toughness and TBC durability has also been found in conventional APS TBCs [7,53–55] as well as ASPS TBCs [45]. Thus, the influence of porosity on toughness in ASPS columnar TBCs seems to merit particular consideration while exploring strategies to tailor TBC microstructures for achieving optimum in-service durability.

4.4. Understanding the role of porosity and different pore classes on toughness and hence lifetime

Under cyclic thermal shock conditions, the coating experiences a temperature gradient primarily through the thickness and this can introduce thermal stresses in the coating [8]. In addition, the thermal expansion mismatch between the bond coat and the top coat creates tensile stresses, especially close to the top coat-bond coat interface [8,56]. Accumulation of these stresses can lead to crack formation and its subsequent propagation in the coating [57]. Once the crack is initiated, it has a propensity to propagate through the coating under the cyclic thermal shock conditions experienced by the TBCs. Hence, a thorough understanding of the role of total porosity and different pore classes on crack initiation and propagation can be invaluable in tailoring the ASPS columnar microstructure to improve durability.

It is known in case of conventional APS TBCs that an increase in porosity is often accompanied by a decrease in toughness [52]. A similar trend was also found in this study (shown in Fig. 12), where the toughness is noted to decrease with increase in total porosity. A strong and nearly inverse linear correlation between total porosity and toughness is apparent in these coatings. In addition to the total porosity, similar trend can be seen for both porosity at/near the inter-columnar spacing

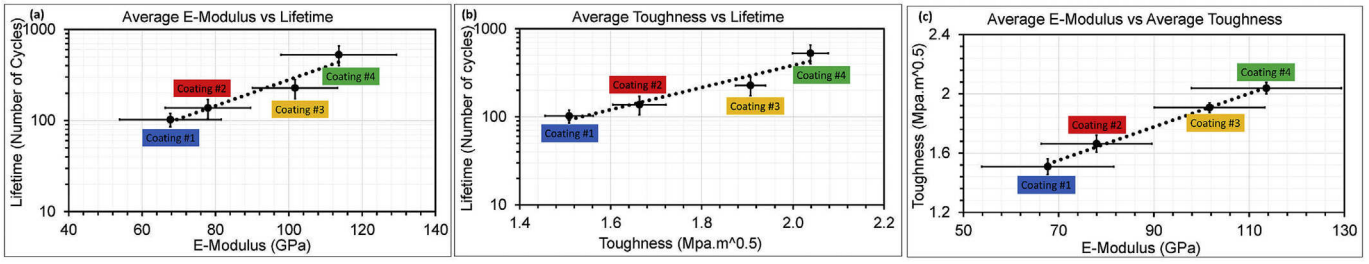

Fig. 11. Dependence of thermal shock lifetime on average E-modulus (a) and average Toughness (b). The relationship between Toughness and E-modulus (c) is also shown.

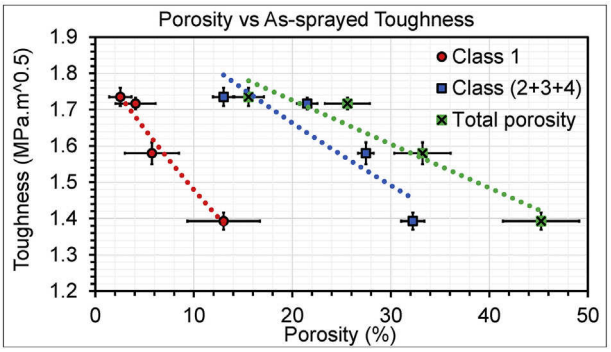

Fig. 12. Relationship between the as-sprayed coatings toughness and porosity within the column (Class-(2 + 3 + 4)), porosity at/near the inter-columnar spacing (Class-1) as well as Total porosity.

(Class-1) as well as within the column (Class-(2 + 3 + 4)) (see Fig. 12). This may now also explain the dependency of lifetime on total porosity and on different pore classes as shown in Fig. 9.

The individual influence of various pore classes on lifetime can be understood by examining the stress intensity factors resulting from the respective pore classes. As stated in literature, higher stress intensity factors can lower the lifetime as it can result in higher crack growth rates [45]. The stress intensity factor (K_I) is proportional to the square root of the defect size [45]. Thus, larger defects in the ceramic layer can lead to higher stress intensities (K_I) and hence higher crack growth rates. Table 3 shows approximate (K_I) values for all the pore classes in each of the as-sprayed coatings, calculated by using a simplified relation in Eq. (7) as reported by Zhou et al. [45] for similar columnar ASPS TBCs:

$$K_I = Y\,\sigma\,\sqrt{c} \;\approx Y\Delta\varepsilon\,E\sqrt{c} \tag{7}$$

Here, c is the equivalent mean pore size (m), E is E-modulus (MPa), Y is the geometry factor (assumed here as 1.13 for spherical pores [45]) and $\Delta\varepsilon$ is the strain (assumed here 0.0025 as suggested in [45] for columnar TBCs). As can be seen from Table 3, the stress intensity factors due to Class-1 pores were significantly higher in all as-sprayed coatings (about 3 times higher than Class-2 and about 6–10 times higher than Class-3 pores) which clearly shows the severity of Class-1 porosity in affecting the lifetime more than other pore classes. Moreover, as previously observed in Section 3.3, Class-1 type porosity changes with time at high temperature (i.e. increased in this study). Such an increase in the Class-1 porosity can also increase the mean Class-1 pore size and the associated stress intensity factor (K_I) as shown in Table 3. This suggests that such coarsening of Class-1 pores can increase the probability for crack initiation and propagation, thereby affecting the thermal shock lifetime significantly.

The stress intensity factors due to Class-4 pores were found to be negligible compared to all other pore classes. This is because of the significantly lower pore size of the Class-4 pores (16 nm–25 nm). In addition, as observed in Section 3.3, the Class-4 porosity (averaged for all the four coatings studied) decreased from about 7% to 2% (see Figs. 5(b) and 6(e)) with time of exposure to high temperature. Therefore, unlike other pore classes, it can be said that the influence of Class-4 porosity on thermal shock lifetime is not as significant as other pore classes. Hence, the role of Class-4 porosity can be ignored while tailoring the microstructure for superior performance.

4.4.1. Crack initiation and propagation

Consistent with the above, all the coatings were found to exhibit horizontal cracks that seemingly initiated at/near the inter-columnar spaces that are the primary regions where Class-1 porosity is located. This is illustrated for Coating #2 and Coating #4 in Figs. 13 and 14 respectively, which clearly establishes the inter-columnar spaces to be the preferential crack initiation regions in ASPS TBCs. Similar observations were also made by Bumgardner et al. in case of dense vertically cracked APS TBCs, where the horizontal cracks were found to initiate at the vertical cracks present throughout the ceramic layer [58]. It is also relevant to point out here that, in addition to the above, there will always be a propensity for the crack once initiated to propagate along a path of least resistance. This could involve the coarse porosity in the vicinity of crack initiation (Class-1 porosity) as more clearly shown in Fig. 13(a-2) and subsequently porosity within the column (Class-(2 + 3 + 4)) as shown in Fig. 13 (a-1 & b-1). Fig. 13 shows an example of propagation of one such crack that eventually bridges with other cracks and leads to spallation/failure of the coating. Such crack bridging can occur either due to intra-columnar crack bridging as shown in Fig. 13(b-1), where two cracks from neighboring inter-columnar spaces can bridge within the column, or due to the inter-columnar crack merging as shown in Fig. 13(a-1), where a through crack within a column can possibly merge with a through crack in the next adjacent column. Moreover, any presence of inter-pass (IP) porosity bands in the coating can also provide an easy path for crack propagation within a column. Such a preferential crack propagation along the inter-pass (IP) porosity bands is clearly visible in case of Coating #4 as shown in Fig. 14.

In order to further strengthen the above observations regarding the preferential crack initiation regions in the columnar microstructures, the hardness was measured within the columns to obtain a horizontal hardness profile. Hardness profiles of all the TBCs, shown in Fig. 15, suggest that the columns are marginally stronger at the center of the column (X-C) than away from the center and closer to the inter-columnar spacing (XI-1 & XI-2) (see Fig. 15(a) and (b) respectively). It should be noted that, a variation of about >50 HV0.1 in hardness, in a column having a width of only about 50 μm–100 μm can be considered significant. The non-uniform porosity distribution within a column can be responsible for such a variation in hardness. This could also be the possible reason that may explain preferential crack initiation at or near the inter-columnar spacing, since it is mechanically a weaker zone within the column.

Figs. 16 (a) and (b) show the micrographs of Coating #2 and Coating #4, respectively, after failure. The crack profile, as marked by black arrows in both the micrographs, clearly shows the crack was deviated at each inter-columnar spacing. Based on this observation, and the above discussion regarding crack initiation and propagation, it can be said that crack initiation and propagation continues through the coating column by column ultimately delaminating the coating from the substrate. Bumgardner et al. in a recently published systematic in-situ study on dense vertically cracked (DVC) APS TBCs have indeed explained such a coating delaminating mechanism. In their study, the ceramic layer was found to delaminate due to bridging, shielding and deflection of these horizontal cracks which initiate at the vertical cracks and the crack

Table 3
Approximate equivalent mean pore size of different pore classes and corresponding stress intensity factors (K_I) in (MPa·m$^{0.5}$) (*negligible values compared to other pore classes).

Coating #	Class-1 (as-sprayed)		Class-1 (after 200 h)		Class-2 (as-sprayed)		Class-3 (as-sprayed)		Class-4 (as-sprayed)	
	Pore size (μm)	K_I	Pore size (μm)	K_I	Pore size (μm)	K_I	pore size (nm)	K_I	pore size (nm)	K_I
1	24	0.9	27	1.1	2	0.3	406	0.1	16	*
2	22	1.0	31	1.6	2	0.3	227	0.1	25	*
3	20	1.3	26	1.4	2	0.4	368	0.2	17	*
4	20	1.2	30	2.1	2	0.4	540	0.2	18	*

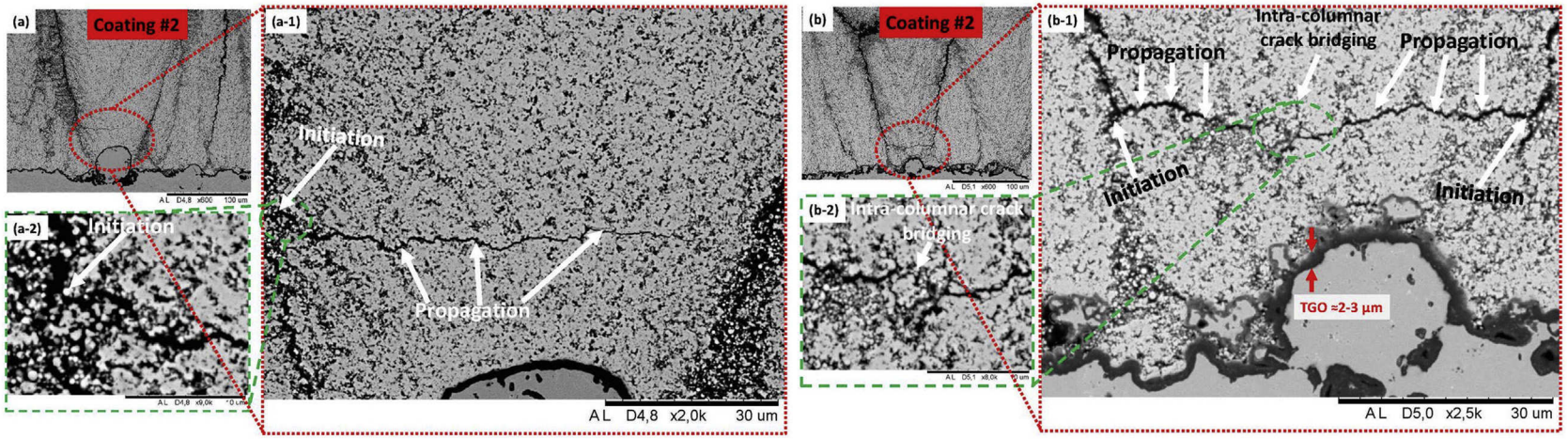

Fig. 13. Crack initiation and propagation in Coating #2, (a, a-1 & a-2) showing a crack initiating at the inter-columnar space and propagating towards the next nearest inter-columnar space; (b, b-1 & b-2) showing the crack initiating at the two neighboring inter-columnar spaces and bridging within the column (intra-columnar crack bridging).

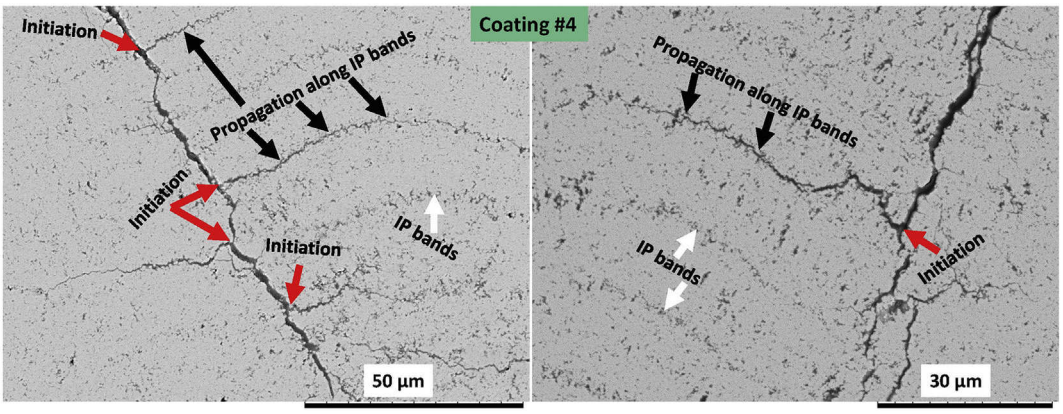

Fig. 14. Magnified micrographs of failed Coating #4 showing the preferential initiation of cracks in the region where inter-pass porosity bands meet the inter-columnar spaces (marked by red arrows) and their subsequent propagation along the inter-pass porosity bands (marked by black arrows).

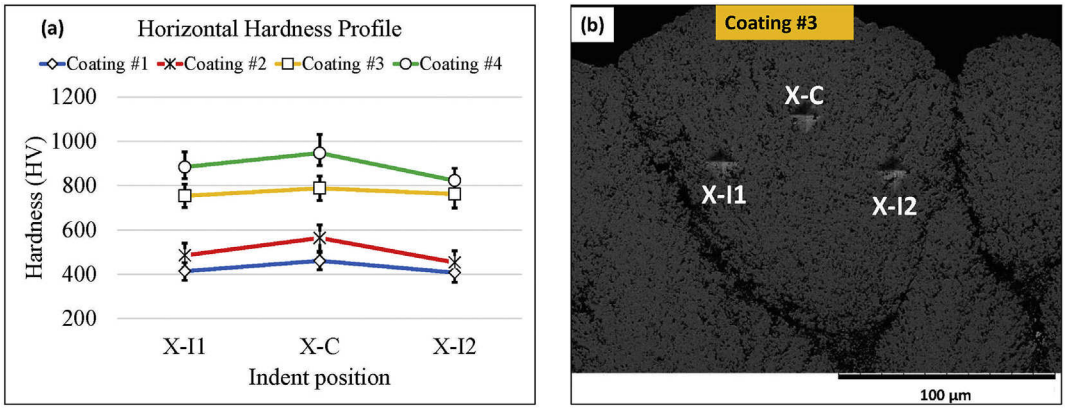

Fig. 15. Horizontal hardness profile measured in all coatings (a) with indents made at the center of the column (X-C) and close to the inter-columnar spacing (X-I1 & X-I2) as shown for Coating #3 (b).

initiation was found to be promoted due to the irregularities or internal defects in the coating such as pre-existing pores, inter-splat boundaries etc. [58].

4.4.2. Minimizing the crack initiation and propagation

In view of the foregoing discussion, reduction in Class-1 porosity during processing can be considered as one of the desirable targets to improve TBC lifetime by reducing the crack initiation sites and stress intensity factors. This can be accomplished by ensuring the presence of a dense and uniform region within the columns immediately adjacent to the inter-columnar spaces, as exemplified by the microstructure of Coating #4 in Fig. 17. In the binary images of Class-1 porosity in Coating #1 and Coating #4 shown in Fig. 17(b-1) and (b-4), respectively, it can be clearly noticed that the region close to the inter-columnar spacing in Coating #4 is significantly denser and uniform with lower porosity compared to Coating #1, where large clusters of pores are present at/near

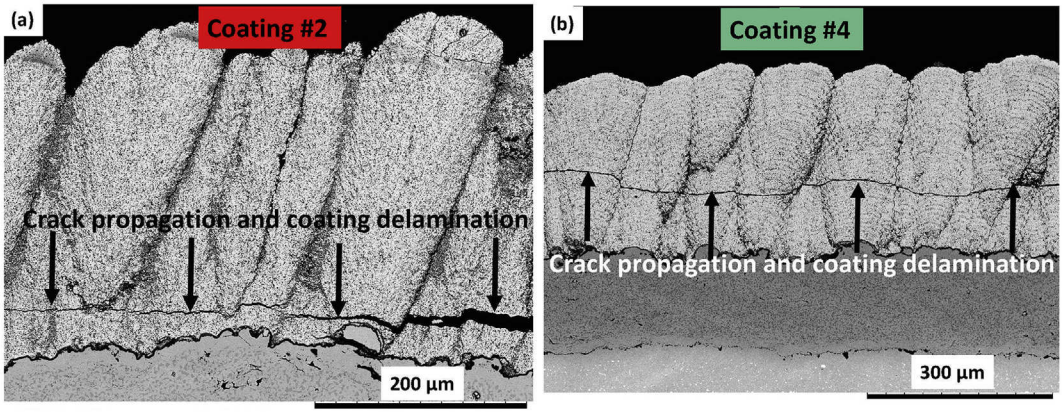

Fig. 16. Crack propagation and coating delamination (marked with black arrows) in failed Coating #2 (a) and Coating #4 (b).

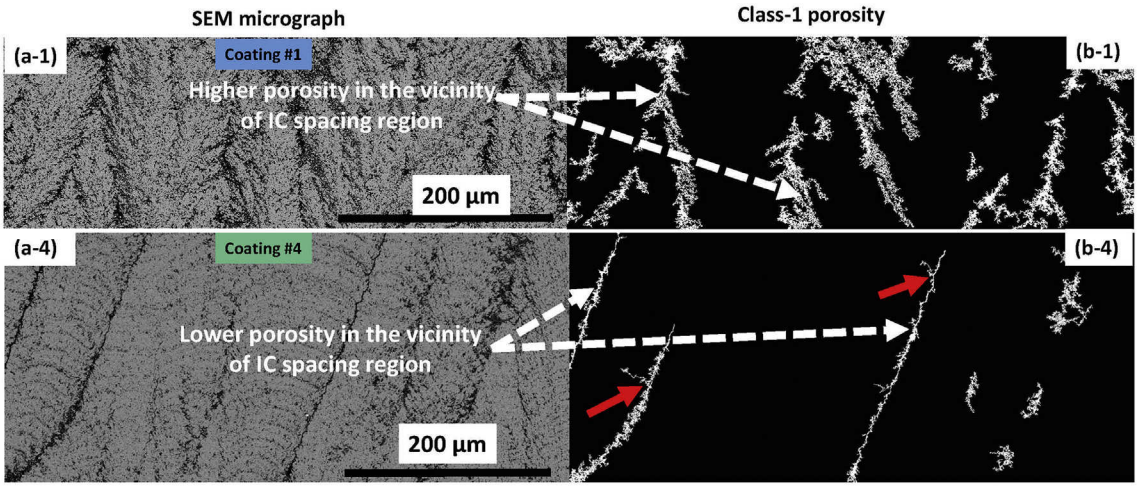

Fig. 17. Binary images of polished cross-section micrographs of Coating #1 (a-1 and b-1) and Coating #4 (a-4 and b-4) showing the difference between the presence of Class-1 porosity in two coatings.

the inter-columnar spacing. This may explain the higher toughness and also the considerably higher lifetime of Coating #4 than Coating #1.

In addition, it is conceivable that eliminating/reducing the inter-pass porosity bands in Coating #4 could have significantly decelerated crack propagation in these coatings and further improved their lifetime. This is because, as mentioned earlier, these inter-pass porosity bands (as marked by red arrows in Fig. 17 (b-4)) act as preferential crack propagation sites during cycling thermal shock test. The failed micrograph of Coating #4 shown in Fig. 14 clearly reveals this and further suggests that the cracks initiate at the regions where the inter-porosity bands meet the inter-columnar space.

Apart from mitigating crack initiation, suppressing crack propagation is also important for TBC durability and can be achieved by ensuring higher toughness in the columns. One approach to accomplish this is by decreasing the porosity within a column (which mainly comprises Class-(2 + 3 + 4) porosity). However, as reported earlier in Section 3.2 and Section 3.3, the percentage contribution of Class-4 porosity with respect to the total porosity is much lower compare to the Class-2 and Class-3 porosity, both in as-sprayed condition and following high temperature exposure and could correspondingly have negligible impact on coating durability. In addition, as mentioned in previous section the resulting stress intensity factors due to Class-4 pores are negligible. Thus, it may be pertinent to focus on suitably tailoring only the Class-(2 + 3) porosity within a column in order to maximize TBC durability.

As found in the previous section, the resultant stress intensity factor due to Class-3 pores were significantly lower (2–3 times) than due to Class-2 pores. This suggests that it can be desirable to completely avoid the Class-2 porosity and retain an optimum amount of Class-3 porosity in order to provide the necessary thermal insulation. Another advantage of retaining Class-3 pores over Class-2 pores is the increased phonon scattering interfaces in case of Class-3 pores than Class-2 pores (for the same amount of Class-2 and Class-3 porosity) which can reduce the thermal conductivity [59]. Definitely, more work is needed to find the optimum number (anything between 10 and 15%) for retaining the Class-3 porosity in such TBCs in order to provide a balance between toughness and conductivity.

4.5. Design strategy for tailoring ASPS columnar microstructure to achieve superior performance

In view of the above, suitable tailoring of porosity in ASPS TBCs could be the pathway to achieve superior coating performance and perhaps the focus of future efforts to optimize the ASPS process. From a design perspective, it is important to tailor the ASPS columnar microstructure in such a way that yields a combination of high thermal shock lifetime and low thermal conductivity. Based on the foregoing discussions, a flow chart summarizing all the important aspects that need to be considered for tailoring the ASPS columnar microstructure to achieve superior performance is given in Fig. 18.

Fig. 18 recommends the desired target levels for each class of porosity that are most likely to yield the much sought after conductivity-lifetime combination. The sources of each class of porosity and the major influencing process parameters that can be used as control factors to manipulate levels of porosity in the four categories are also listed. The figure recommends the presence of optimum Class-1 as well as Class-3 porosity and negligible Class-2 as well as Class-4 porosity and, based on the growing literature and knowledge relating to SPS TBCs, realizing this in due course through process parameter control is conceivable. For example, it can be noted that the presence of Class-1 porosity, which is comprised of both the inter-columnar spaces as well as the coarse porosity typically present in their vicinity (see Fig. 1(d)), is inevitable due to the presence of column gaps in columnar SPS TBCs. Consequently, it was also found in this work that Class-1 porosity increases with column density. Since column density is identified as a life determining factor in case of SPS TBCs [16,24], it is desirable to have an optimum column density to ensure the requisite strain tolerance but avoid the other major sources of Class-1 porosity in the vicinity of the column gap. This can be achieved by controlling the main influencing process parameters, which are listed as control factors in Fig. 18. High plasma power and enthalpy, low feed rate, high total gas flow rate and high spray distance can decrease droplet momentum by reducing the droplet size and/or the velocity at impact and, hence, can increase the column density [18,19,60] (see Section 4.1). In addition, the literature shows that bond coat roughness, as well as suspension properties such as surface tension, viscosity and particle size distribution, can also affect the column density in case of SPS TBCs [13,16].

Like in case of Class-1 porosity discussed above, similar understanding based design philosophy can be utilized in case of all other porosity classes and their respective sources as listed in Fig. 18. The schematic of a suggested tailored columnar microstructure based on the flow chart in Fig. 18 is schematically illustrated in Fig. 19. The proposed microstructure appears to be intermediate between conventional columnar EBPVD and dense vertically cracked APS microstructures, with presence of thin and uniform inter-columnar spaces (Class-1) and submicron intra-columnar pores (Class-3).

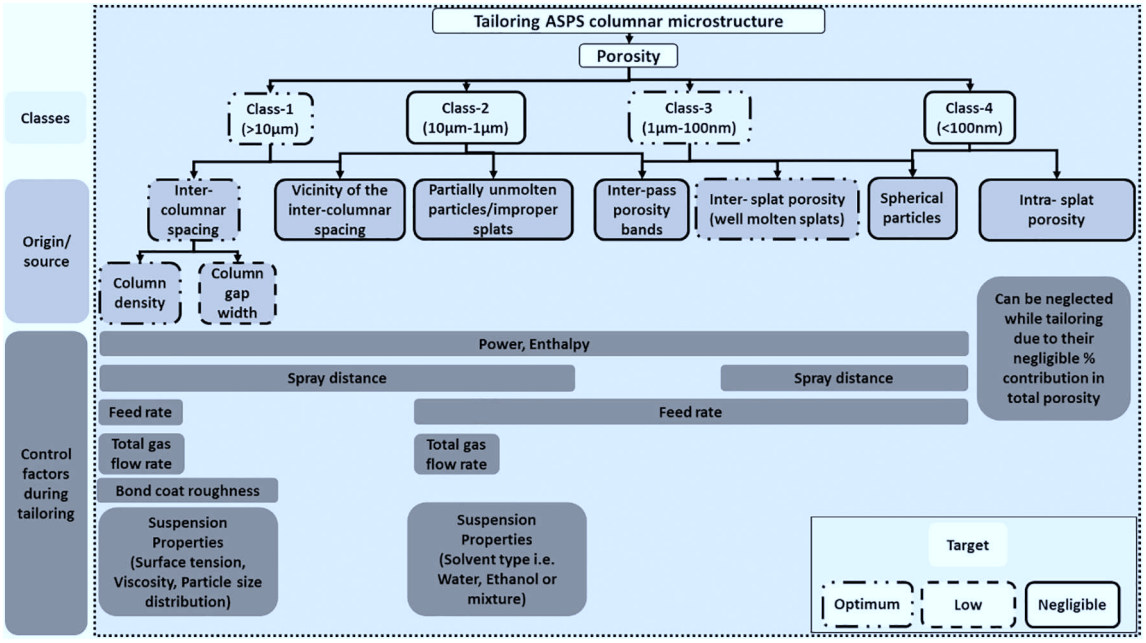

Fig. 18. Flow chart summarizing various important aspects of ASPS columnar microstructure along with different control factors needed to enable tailoring of such microstructures to achieve superior performance.

5. Conclusions

This study was aimed at understanding of the role of porosity on the durability of the rather complex columnar SPS TBCs to serve as the basis for tailoring their columnar microstructures to achieve superior TBC performance. Failure analysis of columnar TBCs subjected to thermal shock test revealed a strong correlation between the total porosity and lifetime, with the lifetime progressively decreasing with increase in total porosity. The porosity was classified in different categories as Class-1 (>10 μm), Class-2 (10 μm–1 μm), Class-3 (1 μm-100 nm), and Class-4 (<100 nm) and their individual influence on thermal shock lifetime was also investigated and found to be related to their corresponding stress intensity factors. In terms of coating properties, the fracture toughness was found to be the most prominent life-determining factor and observed to have a strong correlation, with the durability increasing with toughness. An understanding-based design strategy to tailor the columnar microstructure of SPS coatings to achieve superior performance has been proposed and involves realization of a microstructure with negligible Class-4 and Class-2 porosity, and optimum Class-1 porosity and Class-3 porosity. The available control factors to accomplish such a desired microstructure have also been identified.

Acknowledgements

This work was financially supported by Västra Gotland region, Sweden through a project 'PROSAM' (RUN 612-0974-13). Authors also thank the financial support for open access publication of this work through a project "SiCoMaP+" industrial research school financed by the Knowledge Foundation (DNr 20140130). The authors would like to acknowledge Dr. Nicholas Curry and Mr. Stefan Björklund for helping out with the spraying of coatings. Authors are thankful to Dr. Frantisek Lukac, IPP, Prague and Toni Bogdanoff, Jönköping University for support in conducting the XRD experiment & LFA measurements respectively. Authors would also like to thank an Internship student Mr. Venkateswaran Vaidhyanathan and PhD student Johanna Ekberg from Chalmers for helping out with the image analysis and SEM respectively.

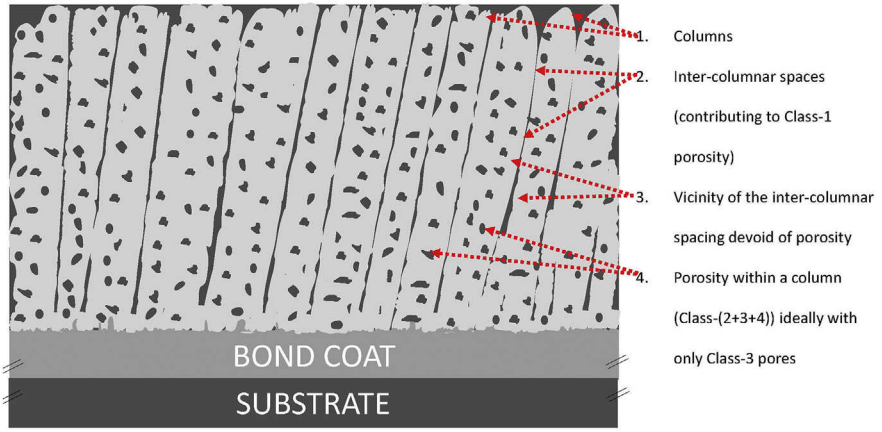

Fig. 19. Schematic of a tailored ASPS columnar microstructure design.

Authors would also like to thank Mr. Dapeng Zhou, IEK-1, Forschungszentrum Jülich, Germany, Mr. William Premnath, University West, Sweden and Dr. Jürgen Malzbender, IEK-2, Forschungszentrum Jülich, Germany for supporting with the characterization of the mechanical properties. Moreover authors also thank Mrs. Sigrid Schwartz-Lückge, IEK-1, Forschungszentrum Jülich, Germany for performing the MIP experiments.

References

[1] R. Vassen, X. Cao, F. Tietz, D. Basu, D. Stöver, Zirconates as new materials for thermal barrier coatings, J. Am. Ceram. Soc. 83 (8) (2000) 2023–2028.
[2] A.D. Jadhav, N.P. Padture, E.H. Jordan, M. Gell, P. Miranzo, E.R. Fuller Jr., Low-thermal-conductivity plasma-sprayed thermal barrier coatings with engineered microstructures, Acta Mater. 54 (12) (2006) 3343–3349.
[3] R.W. Steinbrech, V. Postolenko, J. Monch, J. Malzbender, L. Singheiser, Testing method to assess lifetime of EB-PVD thermal barrier coatings on tubular specimens in static and cyclic oxidation tests, Ceram. Int. 37 (1) (2011) 363–368.
[4] F. Cernuschi, L. Lorenzoni, S. Ahmaniemi, P. Vuoristo, T. Mäntylä, Studies of the sintering kinetics of thick thermal barrier coatings by thermal diffusivity measurements, J. Eur. Ceram. Soc. 25 (4) (2005) 393–400.
[5] R.W. Trice, Y.J. Su, J.R. Mawdsley, K.T. Faber, A.R.D. Arellano-Lopez, H. Wang, W.D. Porter, Effect of heat treatment on phase stability, microstructure, and thermal conductivity of plasma-sprayed YSZ, J. Mater. Sci. 37 (11) (2002) 2359–2365.
[6] A. Rabiei, A.G. Evans, Failure mechanisms associated with the thermally grown oxide in plasma-sprayed thermal barrier coatings, Acta Mater. 48 (15) (2000) 3963–3976.
[7] G. Di Girolamo, F. Marra, C. Blasi, E. Serra, T. Valente, Microstructure, mechanical properties and thermal shock resistance of plasma sprayed nanostructured zirconia coatings, Ceram. Int. 37 (7) (2011) 2711–2717.
[8] A.G. Evans, J.W. Hutchinson, The mechanics of coating delamination in thermal gradients, Surf. Coat. Technol. 201 (18) (2007) 7905–7916.
[9] N. Curry, N. Markocsan, X.-H. Li, A. Tricoire, M. Dorfman, Next generation thermal barrier coatings for the gas turbine industry, J. Therm. Spray Technol. 20 (1–2) (2011) 108–115.
[10] R. Naraparaju, M. Hüttermann, U. Schulz, P. Mechnich, Tailoring the EB-PVD columnar microstructure to mitigate the infiltration of CMAS in 7YSZ thermal barrier coatings, J. Eur. Ceram. Soc. 37 (1) (2017) 261–270.
[11] N. Curry, J. Donoghue, Evolution of thermal conductivity of dysprosia stabilised thermal barrier coating systems during heat treatment, Surf. Coat. Technol. 209 (2012) 38–43.
[12] N. Curry, K. VanEvery, T. Snyder, N. Markocsan, Thermal conductivity analysis and lifetime testing of suspension plasma-sprayed thermal barrier, CoatingsTech 4 (3) (2014) 630–650.
[13] N. Curry, K. VanEvery, T. Snyder, J. Susnjar, S. Bjorklund, Performance testing of suspension plasma sprayed thermal barrier coatings produced with varied suspension parameters, CoatingsTech 5 (3) (2015) 338–356.
[14] J. Oberste-Berghaus, S. Bouaricha, J.-G. Legoux, C. Moreau, Injection conditions and in-flight particle states in suspension plasma spraying of alumina and zirconia nano-ceramicsProceedings of the International Thermal Spray Conference, 2005 (Basel, Switzerland).
[15] K. VanEvery, M.J.M. Krane, R.W. Trice, H. Wang, W. Porter, M. Besser, D. Sordelet, J. Ilavsky, J. Almer, Column formation in suspension plasma-sprayed coatings and resultant thermal properties, J. Therm. Spray Technol. 20 (4) (2011) 817–828.
[16] N. Curry, Z. Tang, N. Markocsan, P. Nylen, Influence of bond coat surface roughness on the structure of axial suspension plasma spray thermal barrier coatings — thermal and lifetime performance, Surf. Coat. Technol. 268 (2015) 15–23.
[17] H. Kassner, A. Stuke, M. Rodig, R. Vassen, D. Stover, Influence of porosity on thermal conductivity and sintering in suspension plasma sprayed thermal barrier coatings, Adv. Ceram. Coat. Interfaces III Ceram. Eng. Sci. Proc. 46 (2009) 147.
[18] A. Ganvir, N. Curry, S. Bjorklund, N. Markocsan, P. Nylen, Characterization of microstructure and thermal properties of YSZ coatings obtained by Axial Suspension Plasma Spraying (ASPS), J. Therm. Spray Technol. 24 (7) (2015) 1195–1204.
[19] A. Ganvir, N. Curry, N. Markocsan, P. Nylen, S. Joshi, M. Vilemova, Z. Pala, Influence of microstructure on thermal properties of axial suspension plasma-sprayed YSZ thermal barrier coatings, J. Therm. Spray Technol. 25 (1–2) (2015) 202–212.
[20] S. Goel, S. Björklund, N. Curry, U. Wiklund, S. Joshi, Axial suspension plasma spraying of Al_2O_3 coatings for superior tribological properties, Surf. Coat. Technol. 315 (2017) 80–87.
[21] S. Björklund, S. Goel, S. Joshi, Function-dependent coating architectures by hybrid powder-suspension plasma spraying: injector design, processing and concept validation, Mater. Des. 142 (2018) 56–65.
[22] B. Bernard, A. Quet, L. Bianchi, A. Joulia, A. Malie, V. Schick, B. Remy, Thermal insulation properties of YSZ coatings: Suspension Plasma Spraying (SPS) versus Electron Beam Physical Vapor Deposition (EB-PVD) and Atmospheric Plasma Spraying (APS), Surf. Coat. Technol. 318 (2017) 122–128.
[23] A. Ganvir, N. Markocsan, S. Joshi, Influence of isothermal heat treatment on porosity and crystallite size in axial suspension plasma sprayed thermal barrier coatings for gas turbine applications, CoatingsTech 7 (1) (2016) 4.
[24] Y. Zhao, D. Li, X. Zhong, H. Zhao, L. Wang, F. Shao, C. Liu, S. Tao, Thermal shock behaviors of YSZ thick thermal barrier coatings fabricated by suspension and atmospheric plasma spraying, Surf. Coat. Technol. 249 (2014) 48–55.
[25] W.Q. Wang, C.K. Sha, D.Q. Sun, X.Y. Gu, Microstructural feature, thermal shock resistance and isothermal oxidation resistance of nanostructured zirconia coating, Mater. Sci. Eng. A 424 (1) (2006) 1–5.
[26] R. Ahmadi-Pidani, R. Shoja-Razavi, R. Mozafarinia, H. Jamali, Improving the thermal shock resistance of plasma sprayed CYSZ thermal barrier coatings by laser surface modification, Opt. Lasers Eng. 50 (5) (2012) 780–786.
[27] H. Jamali, R. Mozafarinia, R. Shoja Razavi, R. Ahmadi-Pidani, Comparison of thermal shock resistances of plasma-sprayed nanostructured and conventional yttria stabilized zirconia thermal barrier coatings, Ceram. Int. 38 (8) (2012) 6705–6712.
[28] D. Thirumalaikumarasamy, K. Shanmugam, V. Balasubramanian, Influences of atmospheric plasma spraying parameters on the porosity level of alumina coating on AZ31B magnesium alloy using response surface methodology, Prog. Nat. Sci.: Mater. Int. 22 (5) (2012) 468–479.
[29] R. Vassen, F. Cernuschi, G. Rizzi, A. Scrivani, N. Markocsan, L. Östergren, A. Kloosterman, R. Mervel, J. Feist, J. Nicholls, Recent activities in the field of thermal barrier coatings including burner rig testing in the European Union, Adv. Eng. Mater. 10 (10) (2008) 907–921.
[30] M. Lawrence, Y. Jiang, Porosity, pore size distribution, micro-structure, Bio-aggregates Based Building Materials, Springer, Dordrecht 2017, pp. 39–71.
[31] ImageJ Software, *Image processing and analysis in java*. [Online]Available: http://imagej.nih.gov/ij/, Accessed date: 17 November 2014.
[32] A. Ganvir, V. Vaidhyanathan, N. Markocsan, M. Gupta, Z. Pala, F. Lukac, Failure analysis of thermally cycled columnar thermal barrier coatings produced by high-velocity-air fuel and axial-suspension-plasma spraying: a design perspective, Ceram. Int. 44 (3) (2017) 3161–3172.
[33] B. Siebert, C. Funke, R. Vassen, D. Stover, Changes in porosity and Young's modulus due to sintering of plasma sprayed thermal barrier coatings, J. Mater. Process. Technol. 92–93 (1991) 217–223.
[34] P.A. Webb, An Introduction to the Physical Characterization of Materials by Mercury Intrusion Porosimetry With Emphasis on Reduction and Presentation of Experimental Data 2 CONTENTS, Micromeritics Instrument Corporation, Norcross, Georgia, 2001.
[35] A. Ganvir, N. Curry, N. Markocsan, P. Nylén, F.-L. Toma, Comparative study of suspension plasma sprayed and suspension high velocity oxy -fuel sprayed YSZ thermal barrier coatings, Surf. Coat. Technol. 268 (2015) 70–76.
[36] A. Macwan, M. Marr, O. Kesler, D.L. Chen, Microstructure, hardness, and fracture toughness of suspension plasma sprayed yttria-stabilized zirconia electrolytes on stainless steel substrates, Thin Solid Films 584 (2015) 23–28.
[37] K. Niihara, R. Morena, D.P.H. Hasselman, Evaluation of KIc of brittle solids by the indentation method with low crack-to-indent ratios, J. Mater. Sci. Lett. 1 (1) (1982) 13–16.
[38] C. Viazzi, J.-P. Bonino, F. Ansart, A. Barnabé, Structural study of metastable tetragonal YSZ powders produced via a sol–gel route, J. Alloys Compd. 452 (2) (2008) 377–383.
[39] C.H. Lee, H.K. Kim, H.S. Choi, H.S. Ahn, Phase transformation and bond coat oxidation behavior of plasma-sprayed zirconia thermal barrier coating, Surf. Coat. Technol. 124 (1) (2000) 1–12.
[40] J.R. Nicholls, K.J. Lawson, A. Johnstone, D.S. Rickerby, Methods to reduce the thermal conductivity of EB-PVD TBCs, Surf. Coat. Technol. 151–152 (2002) 383–391.
[41] R. Vassen, A. Stuke, D. Stöver, Recent developments in the field of thermal barrier coatings, J. Therm. Spray Technol. 18 (2) (2009) 181–186.
[42] J. Fazilleau, C. Delbos, V. Rat, J.F. Coudert, P. Fauchais, B. Pateyron, Phenomena involved in suspension plasma spraying part 1: suspension injection and behavior, Plasma Chem. Plasma Process. 26 (4) (2006) 371–391.
[43] R. Vassen, S. Giesen, D. Stover, Lifetime of plasma-sprayed thermal barrier coatings: comparison of numerical and experimental results, J. Therm. Spray Technol. 18 (5–6) (2009) 835.
[44] S. Mahade, N. Curry, S. Bjorklund, N. Markocsan, P. Nylen, Failure analysis of Gd2Zr2O7/YSZ multi-layered thermal barrier coatings subjected to thermal cyclic fatigue, J. Alloys Compd. 689 (2016) 1011–1019.
[45] D. Zhou, O. Guillon, R. Vaßen, Development of YSZ thermal barrier coatings using axial suspension plasma spraying, CoatingsTech 7 (8) (2017) 120.
[46] W.D. Kingery, Factors affecting thermal stress resistance of ceramic materials, J. Am. Ceram. Soc. 38 (1) (1955) 3–15.
[47] D.P.H. Hasselman, Unified theory of thermal shock fracture initiation and crack propagation in brittle ceramics, J. Am. Ceram. Soc. 52 (11) (1969) 600–604.
[48] T.J. Lu, N.A. Fleck, The thermal shock resistance of solids, Acta Mater. 46 (13) (1998) 4755–4768.
[49] J. Manara, M. Arduini-Schuster, H.-J. Rätzer-Scheibe, U. Schulz, Infrared-optical properties and heat transfer coefficients of semitransparent thermal barrier coatings, Surf. Coat. Technol. 203 (8) (2009) 1059–1068.
[50] A. Bolcavage, A. Feuerstein, J. Foster, P. Moore, Thermal shock testing of thermal barrier coating/bondcoat systems, J. Mater. Eng. Perform. 13 (4) (2004) 389–397.
[51] M. Ranjbar-Far, J. Absi, S. Shahidi, G. Mariaux, Impact of the non-homogenous temperature distribution and the coatings process modeling on the thermal barrier coatings system, Mater. Des. 32 (2) (2011) 728–735.
[52] G. Dwivedi, V. Viswanathan, S. Sampath, A. Shyam, E. Lara-Curzio, Fracture toughness of plasma-sprayed thermal barrier ceramics: influence of processing, microstructure, and thermal aging, J. Am. Ceram. Soc. 97 (9) (2014) 2736–2744.
[53] M. Pourbafrani, R.S. Razavi, S.R. Bakhshi, M.R. Loghman-Estarki, H. Jamali, Effect of microstructure and phase of nanostructured YSZ thermal barrier coatings on its thermal shock behaviour, Surf. Eng. 31 (1) (2015) 64–73.
[54] M.R. Loghman-Estarki, R. Shoja Razavi, H. Jamali, R. Ashiri, Effect of scandia content on the thermal shock behavior of SYSZ thermal sprayed barrier coatings, Ceram. Int. 42 (9) (2016) 11118–11125.

[55] R. Vaßen, M.O. Jarligo, T. Steinke, D.E. Mack, D. Stöver, Overview on advanced thermal barrier coatings, Surf. Coat. Technol. 205 (4) (2010) 938–942.
[56] A.G. Evans, D.R. Mumm, J.W. Hutchinson, G.H. Meier, F.S. Pettit, Mechanisms controlling the durability of thermal barrier coatings, Prog. Mater. Sci. 46 (5) (2001) 505–553.
[57] M.R. Loghman-Estarki, R. Shoja Razavi, H. Edris, M. Pourbafrany, H. Jamali, R. Ghasemi, Life time of new SYSZ thermal barrier coatings produced by plasma spraying method under thermal shock test and high temperature treatment, Ceram. Int. 40 (1) (2014) 1405–1414.
[58] C. Bumgardner, B. Croom, X. Li, High-temperature delamination mechanisms of thermal barrier coatings: in-situ digital image correlation and finite element analyses, Acta Mater. 128 (2017) 54–63.
[59] A. Ganvir, C. Kumara, M. Gupta, P. Nylen, Thermal conductivity in suspension sprayed thermal barrier coatings: modeling and experiments, J. Therm. Spray Technol. 26 (1–2) (2017) 1–12.
[60] B. Bernard, L. Bianchi, A. Malie, A. Joulia, B. Remy, Columnar suspension plasma sprayed coating microstructural control for thermal barrier coating application, J. Eur. Ceram. Soc. 36 (4) (2016) 1081–1089.